INTERFACE

royalsocietypublishing.org/journal/rsif

Research

Cite this article: Gan Y, Quirk K, Boster KAS, Thomas JH, Kelley DH. 2026 A time-dependent, brain-wide model of solute transport in the glymphatic system. *J. R. Soc. Interface* **23**: 20250822.
https://doi.org/10.1098/rsif.2025.0822

Received: 7 August 2025
Accepted: 8 December 2025

Subject Category:
Life Sciences–Physics interface

Subject Areas:
biophysics

Keywords:
cerebrospinal fluid, perivascular spaces, astrocyte endfeet, glymphatic system, solute transport

Author for correspondence:
Douglas H. Kelley
e-mail: d.h.kelley@rochester.edu

THE ROYAL SOCIETY
PUBLISHING

A time-dependent, brain-wide model of solute transport in the glymphatic system

Yiming Gan, Keelin Quirk, Kimberly A. S. Boster, John H. Thomas and Douglas H. Kelley

Mechanical Engineering, University of Rochester, Rochester, NY, USA

YG, 0000-0002-2463-6316; KQ, 0009-0002-1078-9028; KASB, 0000-0001-5178-128X; JHT, 0000-0002-7127-8654; DHK, 0000-0001-9658-2954

The flow of cerebrospinal fluid (CSF) through the perivascular spaces (PVSs) and interstitial fluid (ISF) in the extracellular space (ECS) is important for brain waste removal and drug delivery. The circulation of this flow is often called the glymphatic system. We build on an existing hydraulic network model of steady flow in this system to enable the study of time-dependent flows, allowing the modelling of the processes of tracer injection and drug delivery in the glymphatic network. Using flow rates from the steady-state model and the method of Laplace transforms, we solve this time-dependent advection–diffusion equation for the network semi-analytically and show that the solution closely matches numerical simulations. We find that a particular value of the endfoot gap cavity fraction maximizes solute perfusion. Furthermore, we find that a smaller gap fraction around PVS segments at the brain surface and a larger gap fraction around deeper PVS segments produce more uniform perfusion, which is consistent with a previous study (Wang *et al.* 2021 *Glia* **69**, 715–728 (doi:10.1002/glia.23923)). We also observe that greater permeability of the ECS improves perfusion, and that tracers with lower diffusivity exhibit enhanced perfusion.

1. Introduction

Cerebrospinal fluid (CSF) flow in perivascular spaces (PVSs) and possibly interstitial fluid (ISF) flow in extracellular spaces (ECSs) play a vital role in clearing protein waste from the brain. Metabolic waste produced by brain tissue is partially transported and removed by these fluids through advection and diffusion. This waste clearance system is often called the glymphatic system. The CSF inflow in the PVSs is hypothesized to exchange with the interstitial or extracellular fluid via bulk flow through aquaporin-4 channels on astrocytic endfeet and the inter-endfoot gaps lining the outer wall of the PVSs, followed by an efflux of fluid along the perivenous spaces, meningeal lymphatics or the subarachnoid space (SAS) [1–3]. Beyond the brain, the CSF pathway extends into the spinal cord, where CSF flows through PVSs and SASs surrounding the spinal vasculature. Similar transport pathways have also been identified in the optic nerve, retina and the hearing system [4,5]. Additionally, CSF flow offers a promising route for drug delivery to treat neurodegenerative diseases, providing a pathway for drugs that cannot cross the blood–brain barrier. Measurements of CSF flow typically rely on tracer injection experiments (especially for penetrating PVSs). Consequently, modelling solute transport within the glymphatic system is essential for tracer-based flow measurements and for optimizing cerebral drug delivery.

Several brain-wide models have been developed to study the flow characteristics in PVSs [6–8]. Using a branching tree model of PVSs and the surrounding parenchyma, the model developed by Tithof *et al.* [6] predicts fluid flow rates by estimating the hydraulic resistances of branching pathways, accounting for interconnected loops present in the pial (surface) vasculature [9]. A global

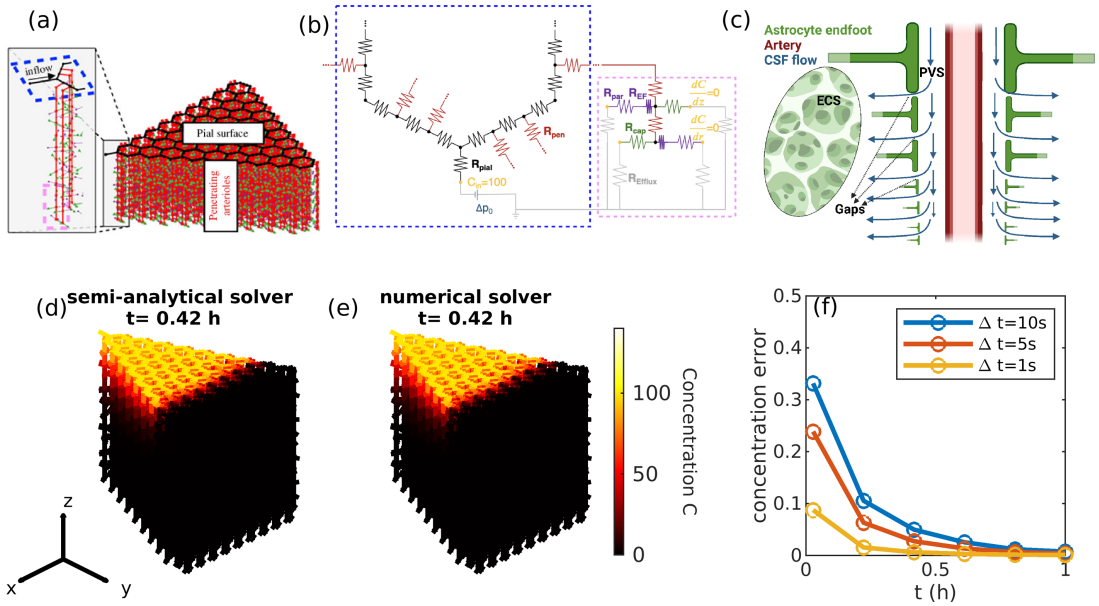

Figure 1. Sketch of the network model and verification of the semi-analytical solution. (a) The modelled perivascular geometry, with colours indicating different segment types, adapted from [6]. Blue and pink dashed lines surround the model regions that are enlarged in (b). (b) Hydraulic resistances model pial PVSs (black), penetrating PVSs (red), all other segments and the efflux routes (grey). Capillary PVSs (green) and parenchymal segments (purple) branch from each penetrating PVS. (c) Sketch of the endfoot wall, which separates the PVS of the penetrating artery from the surrounding ECS. Gaps between endfeet provide the potential pathway for fluid and solute exchange between the two fluid domains. Created with BioRender. The models are tested using a 9-generation hexagon model [9]. (d,e) Solute distribution at $t = 0.42$ h, using the semi-analytical solver and the numerical solver using a time step $\Delta t = 1$ s, both with a steady inlet concentration of $C = 100$ and inlet pressure of $p = 6.6$ Pa (0.05 mmHg). (f) The maximum error between the semi-analytical solution and the numerical solution decreases with decreasing Δt.

pressure drop was applied to reproduce previously measured velocities at the brain's surface. Quirk *et al.* [10] extended the model to solve for steady-state solute transport in the PVSs and the surrounding parenchyma. This extended model helps to determine the spatial distribution of solute in a steady state, to explore the roles of important parameters and to inform future experiments. However, neither of these models incorporates time-dependent solute transport within the network of the glymphatic system.

Efficient clearance and nutrient transport in the brain require adequate perfusion throughout the entire cortical depth. First-principles analysis suggests that, in a large organ like the brain, insufficient perfusion results in non-uniform solute distribution and waste accumulation—conditions incompatible with healthy brain function [3,11]. One way to measure perfusion in the brain is tracer injection experiments. Tracer entry into PVSs depends on molecular size and weight: larger molecules are often restricted to the SAS, whereas smaller solutes penetrate deeper into the cortex. Experiments have demonstrated that dextrans with molecular weights of 2000 kDa or less enter cortical PVSs [12], but larger luminescent particles do not [13]. Numerous experimental studies in both humans and mice have shown that small tracers injected into CSF penetrate beneath the brain's surface, leading to nearly uniform CSF perfusion throughout the cortical depth [6,14–17]. That finding aligns with the intuitive expectation that cells of the same type have similar needs for waste removal, regardless of their location in the brain, so CSF perfusion should be uniform.

While a low-resistance fluid pathway facilitates solute influx, a balanced distribution of resistance within the network may promote more uniform perfusion, ensuring efficient solute delivery throughout the brain. Resistance is provided in part by the astrocyte endfeet that form the outer boundaries of penetrating PVSs, with gaps between endfeet thought to facilitate fluid exchange between the PVSs and surrounding parenchyma (figure 1c). Wang *et al.* [18] measured the distribution of endfoot gaps around penetrating arteries, finding that PVS walls around smaller vessels have greater gap length per unit wall area. That is, as vessels narrow, individual endfeet decrease in size, so more endfeet are required to cover a PVS wall of the same area, resulting in a higher density of gaps. Assuming that distal vessels are narrower, we would expect gaps to cover a greater portion of the perivascular wall in deeper brain regions. Those authors noted that this gap distribution leads to a corresponding decrease in flow resistance with depth, thereby sustaining a uniform CSF flux through the endfoot gaps. Additionally, Tithof *et al.* [6] highlighted that for solutes to reach deeper brain regions rather than leaking into the parenchyma near the surface, the flow resistance in the penetrating PVS must be substantially lower than that of the parenchyma. We carried out simulations with the solute transport model to study these effects.

In this study, we extend the capabilities of the solute transport model developed by Quirk *et al.* [10] to study time-dependent transport within the network. We employ a semi-analytical solution using the Laplace transform for one-dimensional (1D) solute transport with a given steady CSF flow velocity. We account for Taylor dispersion in the PVSs by incorporating enhanced diffusivities in the axial direction [19,20]. We show that the solutions closely match results from a numerical solver based on the spectral method. The semi-analytical approach offers a fast and accurate algorithm for computing solute concentration at any given time and location.

We find that a particular value of the endfoot gap cavity fraction maximizes solute perfusion. Furthermore, we find that a smaller gap fraction around PVS segments at the brain surface and a larger gap fraction around deeper PVS segments produce

more uniform perfusion, consistent with the model proposed by Wang *et al.* [18]. We also observe that greater permeability of the ECS improves perfusion, consistent with the findings of Tithof *et al.* [6] and that tracers with lower diffusivity exhibit enhanced perfusion.

2. Methods

2.1. Governing equations

The model represents the network of PVSs in the territory of the middle cerebral artery on the surface of the mouse brain and the penetrating PVSs that extend from it. For completeness, the model also includes capillary PVSs extending from penetrating PVSs. The existence of capillary PVSs is the subject of an ongoing debate, but at least one recent study presented evidence for them [21]. The simplified network geometry of pial channels arranged in hexagonal loops and connected to penetrating channels was proposed by [22] to capture key aspects of cerebral blood flow. Later, the model was updated to simulate flow through the PVSs surrounding these blood vessels [6]. The PVSs of the penetrating artery are modelled as open space, equivalent to an effective permeability of 1.9×10^{-12} m^2 [6]. The PVSs of the precapillary spaces are modelled as porous media. Within these PVSs, solute transport is governed by the time-dependent advection–diffusion equation:

$$\frac{\partial C}{\partial t} + u\frac{\partial C}{\partial z} = D\frac{\partial^2 C}{\partial z^2}, \tag{2.1}$$

where C is the local concentration, t is the time, z is the axial coordinate, u is the cross-sectional average axial flow speed in the PVS and D is the diffusivity of the solute at that location.

Fluid exchange between PVSs and the parenchyma occurs through the outer boundary of the PVSs of the penetrating arteries. This continuous fluid exchange is expected to depend on local pressure and permeability and therefore to vary with depth. To simplify this exchange and enable an analytical solution, we consider 11 parenchymal branches that are evenly spaced along the z direction of a penetrating artery. The pressure profile is then linear between each pair of adjacent branches but nonlinear from the top down to the end of the penetrating PVS, due to the fluid loss through the branches. (A similar quasi-linear simplification has been made to estimate compressible channel flow, where the pressure drop over a short distance is quasi-linear, but the overall pressure drop is nonlinear [23].) We model the parenchyma as a porous medium and assume that the flow there follows 1D Darcy's law. This model is based on the assumptions that the arterial PVSs are long and straight and that the surrounding parenchyma is axially symmetric around each PVS. As a result, the equation governing flow in the parenchyma is 1D, with the solution given by $\mathbf{u} = q\hat{\mathbf{r}}/2\pi r$, where $\mathbf{u}$ is the (superficial) fluid velocity, q is the volume flow rate per axial length of PVS, $\hat{\mathbf{r}}$ is the unit vector in the cylindrical radial direction and r is the cylindrical radial coordinate (with $r = 0$ at the PVS centreline) [10,24]. In the parenchyma, the time-dependent advection and diffusion equation reads

$$\frac{\partial C}{\partial t} + \frac{q}{2\pi r}\frac{\partial C}{\partial r} = D_{\text{eff}}\frac{1}{r}\frac{\partial C}{\partial r} + D_{\text{eff}}\frac{\partial^2 C}{\partial r^2}, \tag{2.2}$$

where $D_{\text{eff}} = D/\lambda^2$ is the effective diffusivity in the porous ECS and $\lambda = 1.20$ is the tortuosity of the ECS [25]. The nonlinear pressure profile along the PVS converges as the number of parenchymal branches per penetrating PVS increases. It approaches the pressure profile obtained from a two-dimensional (2D) simulation in which fluid loss through endfoot gaps is modelled as a continuous leakage along the PVS, thereby justifying our 1D simplification (figure 9 in appendix D).

2.2. Boundary conditions

To model solute injection, we specify the solute concentration $C = C_0(t)$ in the most proximal pial PVS (the inlet; refer to the PVS segment in the blue dashed box in figure 1a). We set $\partial C/\partial z = 0$ at the outlet of the capillary PVSs and $\partial C/\partial r = 0$ at the outlet of the parenchyma, which ensures that all tracers are carried away by pure advection there. The outlet of the parenchyma is ambiguous, as glymphatic efflux is not yet well characterized; the potential outlet could correspond to the meningeal lymphatic vessels, SASs, perivenous spaces and/or periarterial basement membranes [26]. Here, the distance between the inlet and the outlet of the parenchyma is defined as the median arteriole-to-venule distance [6,9,22,27].

At junctions in the model, concentration is required to be continuous and solute influx is required to equal solute efflux. The solute flux along the ith PVS is given by

$$J_i = S_i\left(C_i u_i - D_i\frac{\partial C_i}{\partial z}\right), \tag{2.3}$$

where S_i is the cross-sectional area through which the solute passes, and other symbols are as defined above, with the subscript i indicating which PVS is being considered. The outer boundary of a penetrating PVS is composed of astrocyte endfeet, and gaps between endfeet may allow fluid and solute transport between the PVS and the parenchyma (figure 1c) [18]. In that case, the solute flux into the ith parenchymal node is given by

$$J_i = F_c s_i\left(C_i u_i - D_i\frac{\partial C_i}{\partial r}\right), \tag{2.4}$$

where F_c is the endfoot gap cavity fraction, s_i represents the surface area of the PVS segment and $F_c s_i$ represents the total area of the gaps on that segment.

We impose the condition that the total solute flux entering a junction (bifurcation) equals the total solute flux exiting that junction. At pial bifurcations, some solute efflux is due to CSF escaping into the SAS, as set by J_{pial}, the fraction of fluid that escapes. We assume pure advection in those efflux routes given that the Péclet number there is high.

2.3. Semi-analytical solution using Laplace transforms

To calculate solute transport, we use the Laplace transform of the concentration in time:

$$\hat{C}(s) = \mathcal{L}(C(t), t) = \int_0^\infty C(t)\mathrm{e}^{-st}\,\mathrm{d}t, \tag{2.5}$$

where $s = \gamma + i\omega$ is a complex frequency with $\gamma > 0$. Both $\hat{C}(s)$ and $C(t)$ can vary spatially. First, considering PVSs, the Laplace transform of equation (2.1) is

$$s\hat{C} + u\frac{\partial \hat{C}}{\partial z} - D\frac{\partial^2 \hat{C}}{\partial z^2} = 0. \tag{2.6}$$

The analytical solution for $\hat{C}$ can be expressed as

$$\hat{C}(z, s) = K_1\mathrm{e}^{z\left(\frac{u}{2D} - \frac{\sqrt{u^2+4sD}}{2D}\right)} + K_2\mathrm{e}^{z\left(\frac{u}{2D} + \frac{\sqrt{u^2+4sD}}{2D}\right)}, \tag{2.7}$$

where K_1 and K_2 are coefficients determined by the boundary conditions. Now, considering the parenchyma, the Laplace transform of equation (2.2) is

$$s\hat{C} + \frac{\frac{q}{2\pi} - D_{\text{eff}}}{r}\frac{\partial \hat{C}}{\partial r} = D_{\text{eff}}\frac{\partial^2 \hat{C}}{\partial r^2}. \tag{2.8}$$

The analytical solution for $\hat{C}$ can be expressed as

$$\hat{C}(r, s) = A_1\left(r\sqrt{-\frac{s}{D_{\text{eff}}}}\right)^k J_k\left(r\sqrt{-\frac{s}{D_{\text{eff}}}}\right) + A_2\left(r\sqrt{-\frac{s}{D_{\text{eff}}}}\right)^k Y_k\left(r\sqrt{-\frac{s}{D_{\text{eff}}}}\right), \tag{2.9}$$

where $k = q/(4\pi D_{\text{eff}})$ and J_k and Y_k represent kth-order Bessel functions of the first and second kind, respectively. A_1 and A_2 are coefficients determined by the boundary conditions. Details about the derivation of these solutions are included in the appendix.

For the case of steady tracer injection, the boundary condition at the inlet reads

$$C_{\text{in}} = C_0 \quad \text{when } t \geq 0, \tag{2.10}$$

where C_{in} is the concentration at the inlet of the network and C_0 is a constant concentration. We set $C = 0$ elsewhere in the network as the initial condition. The Laplace transform of equation (2.10) is

$$\hat{C}_{\text{in}}(s) = \frac{C_0}{s}. \tag{2.11}$$

For the case where the tracer injection stops at time T, we specify

$$\begin{cases} C_{\text{in}} = C_0 & \text{when } 0 \leq t < T, \\ C_{\text{in}} = 0 & \text{when } T \leq t. \end{cases} \tag{2.12}$$

The Laplace transform of equation (2.12) is

$$\hat{C}_{\text{in}}(s) = \frac{C_0(1 - \mathrm{e}^{-Ts})}{s}. \tag{2.13}$$

At the outlet of the capillary PVS, we set the concentration gradient equal to zero:

$$\frac{\partial \hat{C}_{\text{out}}}{\partial z} = 0. \tag{2.14}$$

At the outlet of the parenchyma (perivenous space), we also set the concentration gradient equal to zero:

$$\frac{\partial \hat{C}_{\text{out}}}{\partial r} = 0. \tag{2.15}$$

These conditions establish that solute transport at these outlets occurs purely by advection.

The equations above form a system of linear equations, which we solve in matrix form in MATLAB, as described in [10]. From the solution in the Laplace domain, we obtained the solution in the time domain using a numerical technique for inverting the Laplace transform [28].

Table 1. Parameter values used in the model.

parameter	symbol	value
pial PVS area ratio [29]	Γ_{pial}	1.4
pial artery segment length [9]	l_{pial}	175 µm
pial artery diameter [9]	d_{pial}	46 µm
penetrating PVS area ratio [29]	Γ_{pen}	1.4
penetrating arteriole length [9]	l_{pen}	1000 µm
penetrating arteriole diameter [9]	d_{pen}	11 µm
penetrating permeability [9]	κ_{pen}	nan (open) m^2
capillary PVS area ratio [30]	Γ_{cap}	0.07
effective capillary length [6]	l_{cap}	200 µm
capillary PVS permeability [6]	κ_{cap}	1.8×10^{-14} m^2
capillary PVS diameter [31]	d_{cap}	6 µm
parenchyma permeability [32,33]	κ_{par}	1×10^{-17} to 5×10^{-15} m^2
endfoot wall thickness [34]	T	0.45 µm
endfoot gap [35]	g	20 nm
endfoot wall cavity fraction [34,36]	F_c	0.003–0.370
dynamic viscosity [37]	μ	6.9×10^{-4} Pa s^{-1}
median arteriole-to-venule distance [9,33]	L	128 µm
tracer diffusivity [12]	D	10–2000 µm^2 s^{-1}
tortuosity [38]	λ	1.20

2.4. Verification of the semi-analytical solution

The semi-analytical solution was shown to closely match results from a numerical solver, described in the appendix. We performed the simulation using both methods on a hexagon model with nine generations of vessels [6] and extracted the solute profile at a few times (figure 1d,e). We found good agreement between the two methods. The relative error between the semi-analytical solution and the numerical solution decreased as we decreased the time step (Δt) used for the numerical solution (figure 1f), demonstrating the accuracy of the semi-analytical solution. The analytical solution remains valid regardless of whether advection or diffusion is the dominant transport mechanism. In particular, it holds for a diffusivity as low as $D = 1$ µm^2 s^{-1} and a velocity as high as $u =$ 200 µm s^{-1}, well beyond the advective limits reached in tracer experiments. The model parameters and their numerical values are listed in table 1.

3. Results

3.1. Proper gap cavity fraction may optimize solute perfusion

Prior modelling concluded that the flow speeds observed *in vivo* require the glymphatic system to have low overall hydraulic resistance, but also that glymphatic perfusion can be uniform only if other parts of the system have much higher resistance than the PVSs [6]. It has been suggested that gaps between astrocyte endfeet provide a pathway for fluid and solute exchange between PVSs and parenchyma [18], as sketched in figure 1c. If they do, the need for fast flow would favour low-resistance gaps, but the need for good perfusion would favour high-resistance gaps. Resistance depends inversely, and sensitively, on gap fraction. Gap fraction also strongly affects solute flux, according to equation (2.4). Since gap fraction seems to play an important role in the competing requirements of the glymphatic system, we set out to model fluid flow and solute transport while varying the gap fraction.

First, we simulated steady injections with different gap fractions, keeping them uniform throughout the PVS network. With a small gap fraction of 0.1%, tracer entering from the most proximal PVS (the inlet) reached deep brain regions, but the total amount of tracer in the network was small (figure 2a). In contrast, with a large gap fraction of 32%, tracer concentration was high in the pial PVSs (figure 2c), but little tracer reached deeper regions. With a moderate gap fraction of 0.4%, we observed high concentrations in both the pial PVSs and deeper brain regions (figure 2b). Figure 2d shows that as the gap fraction increased, the mean concentration in the network (excluding pial PVSs) first increased and then decreased. The blue dashed line represents the total flow resistance of the parenchyma, which consists of endfoot gap resistance ($R_{endfoot}$) and the ECS resistance (R_{ECS}). In the range where the mean concentration increased with increasing gap fraction, total flow resistance dropped sharply, indicating enhanced

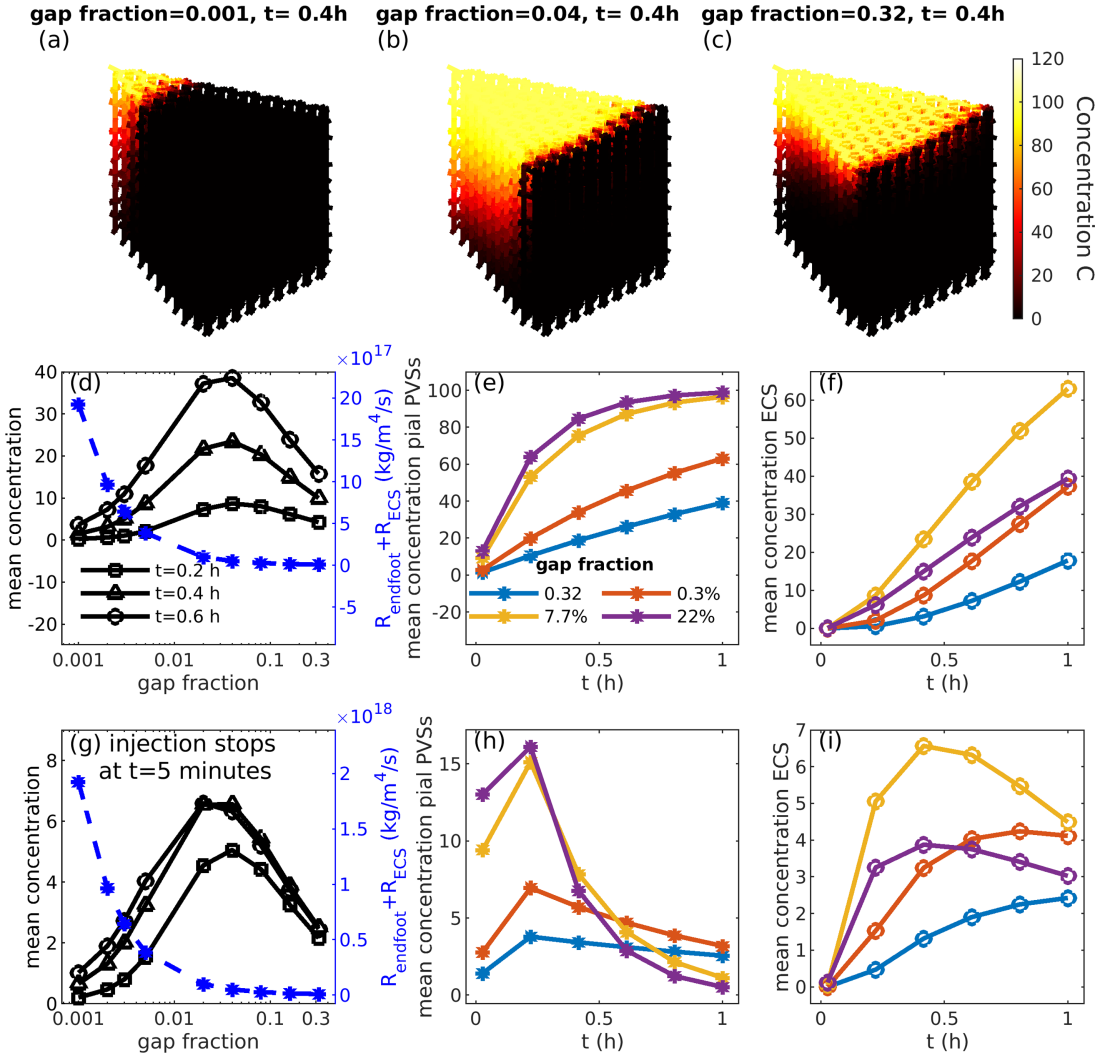

Figure 2. Perfusion with varying gap fractions. (a) In simulations of steady injection, with a small gap fraction of 0.1%, tracer penetrates deeply, but little tracer enters the network. (b) With a moderate gap fraction of 4%, tracer penetrates deeply and much more enters the network. (c) With a large gap fraction of 32%, the mean concentration near the pial surface is high, but little tracer enters deep regions. (d) As gap fraction increases, the mean tracer concentration below the pial PVSs first increases and then decreases, peaking at a 4% gap fraction. The total flow resistance of the parenchyma (including endfoot wall and ECS) decreases with gap fraction. (e) The mean concentration in pial PVSs increases over time and increases more quickly when the gap fraction is greater. (f) Among four values of gap fractions, the mean concentration below the pial PVSs increases over time and increases most quickly with a moderate gap fraction of 7.7%. (g–i) Simulations of time-dependent injections yield similar conclusions.

flow and solute transport. In contrast, when the mean concentration declined with increasing gap fraction, the total flow resistance remained nearly constant because $R_{ECS} \gg R_{endfoot}$ when the gap fraction is large.

Figure 2e shows that the mean concentration in the pial PVSs increased with increasing mean gap fraction. The mean concentration in the network, excluding the pial PVSs, was highest with a moderate gap fraction (figure 2f). Similar trends were observed in time-dependent injection simulations (figure 2g–i). Tracer clearance was faster when the flow resistance was lower (large gap fraction). After injection ceased at $t = 0.5$ h, simulations with larger gap fractions showed lower concentration in the pial PVSs (figure 2h) and slower increase (or even a decrease) of concentration elsewhere (figure 2i), as efflux took over.

3.2. Improved perfusion when gap fraction increases with depth

According to the measurements of Wang *et al.* [18], the gap cavity fraction increases monotonically with arterial diameter. Since the penetrating artery diameter decreases with brain depth, and the number of bifurcated arteries increases [22], it is reasonable to assume that the gap fraction increases monotonically with depth (figure 3a). Those authors also suggested that this gap distribution helps maintain near-uniform perfusion, in that the rate of flow from PVSs to the parenchyma is nearly independent of tissue depth. Here, we compare solute transport simulations with such gap fraction distributions to simulations with a constant gap fraction while keeping the mean gap fraction the same (15%). We set a steady inlet concentration of $C_0 = 100$ and an inlet pressure of 6.6 Pa (0.05 mmHg, corresponding to a flow velocity of ≈ 40 μm s^{-1}, which varies slightly for simulations of different gap distributions).

We varied the gap cavity fraction in proportion to the first, second and third powers of depth and compared these cases to simulations with a constant gap cavity fraction, ensuring the same mean value across all scenarios. By definition, a higher power

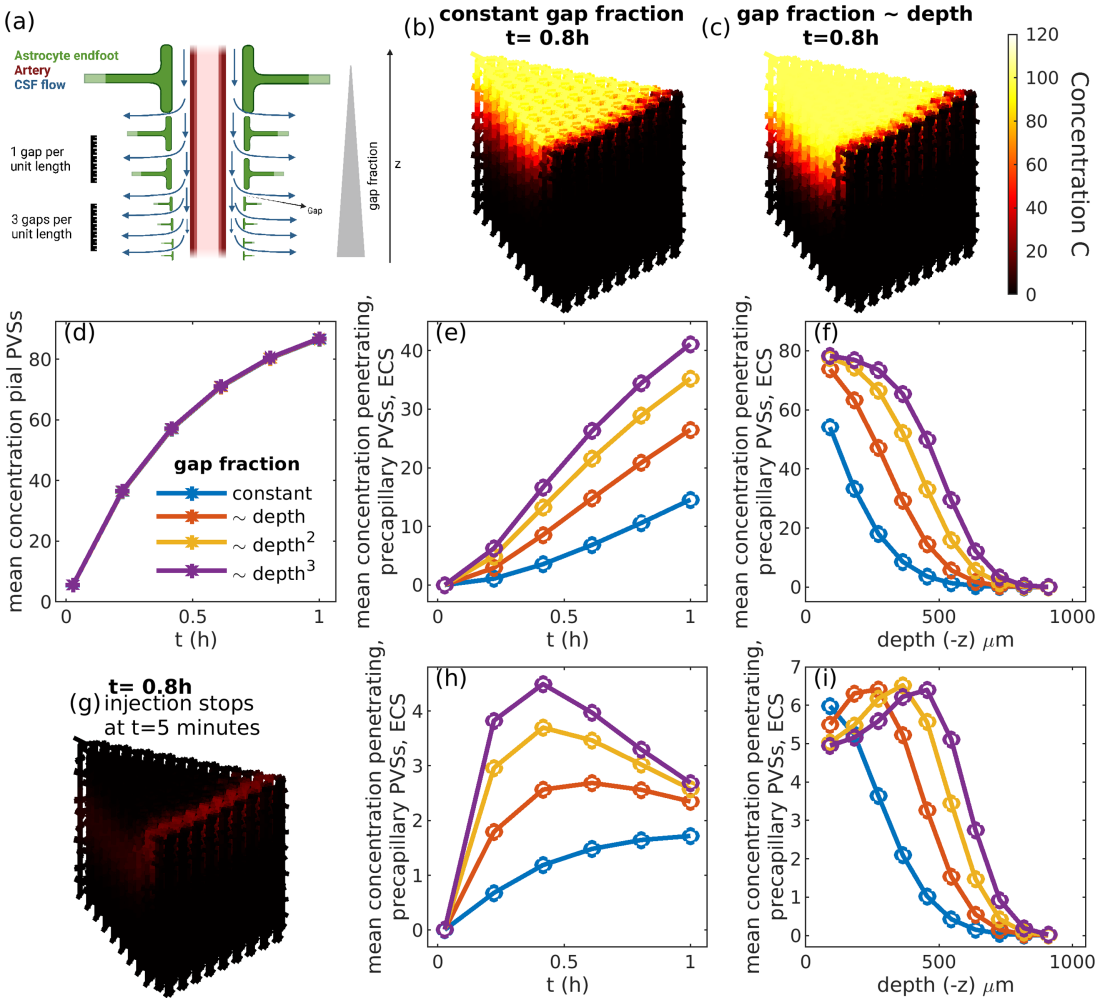

Figure 3. Perfusion with varying gap fraction distribution. (a) Illustration of gap fraction that increases with depth, created using BioRender. (b) Solute distribution at $t = 0.8$ h for a simulation where gap fraction is constant and injection is steady. (c) Solute distribution at $t = 0.8$ h for a simulation where gap fraction increased linearly with depth. We compared the constant gap fraction case to cases in which the gap fraction varied proportionally with the first, second and third powers of depth. The mean concentrations in the pial PVSs were nearly identical in all cases (d), but the mean concentrations in the rest of the network (including the penetrating PVSs, precapillary PVSs and ECS) increased with the power index (exponent) (e). (f) The concentration deep in the tissue was higher when gap fraction increased more sharply with depth. (g) We performed time-dependent injection simulations, where we set the inlet concentration $C_0 = 100$ at $t < 5$ min and $C = 0$ at $t \geq 5$ min. (h,i) We found higher tracer concentration in the network with a gap fraction that monotonically increased with depth.

index (exponent) implies that gap fraction increases more rapidly with depth. With a constant concentration at the network inlet, tracer penetrated deeper in a simulation where the gap cavity fraction increased with depth (figure 3c) than in one where it did not (figure 3b). That observation fits our intuition that small gaps near the surface would tend to prevent tracer from escaping PVSs there, instead allowing it to be transported deeper along penetrating PVSs.

Varying the power index of the gap distribution in simulations of steady injections, we found that the mean concentration in the pial PVSs remained nearly unchanged (figure 3d), but concentration elsewhere increased more rapidly over time if the power index was larger (figure 3e). Additionally, increasing the power index led to a greater accumulation of tracer in deeper brain regions (figure 3f). Similar trends were observed in simulations where injections were stopped after 5 min, following a typical experimental protocol [12] (figure 3g–i).

3.3. Evaluating perfusion with centroid and standard deviation

We evaluated perfusion with two quantities: the centroid of tracer mass and the normalized standard deviation of the tracer concentration within the network. The location of the centroid is

$$\vec{r}_c = (x_c, y_c, z_c) = \frac{\sum_{i=1}^{n} \bar{C}_i \vec{r}_i}{\bar{C}}, \tag{3.1}$$

where n is the total number of segments, $\bar{C}_i$ *is* the average concentration in the ith segment, $\vec{r}_i$ *is* the geometric centroid of the ith segment and $\bar{C}$ is the volumetric average concentration of the entire network. Since we simulate tracer injection from the surface, good perfusion is typically indicated by a centroid located deeper in the tissue (smaller z_c). The coordinate system is illustrated in figure 1, where the x- and y-axes define the lateral plane of the network, with the y-axis serving as the approximate axis of symmetry, and the z-axis oriented opposite to the direction of brain depth. Similarly, good perfusion implies a more uniform tracer

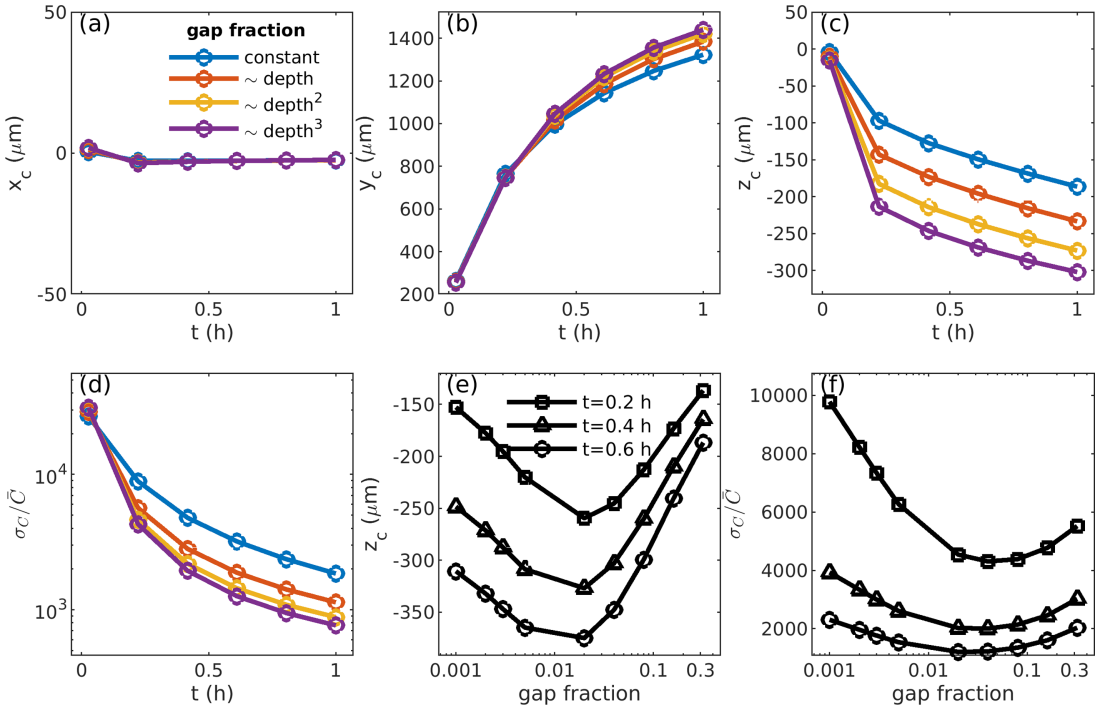

Figure 4. Evaluating perfusion with tracer centroid and spatial standard deviation. (a) In simulations of steady injection, the tracer centroid remained on the approximate centreline of the system ($x_c = 0$) regardless of time and gap distribution, as expected from symmetry. (b) The tracer centroid advanced laterally from the inlet over time, advancing more quickly when gap fraction depends more strongly on depth. (c) The tracer centroid penetrated deeper into the tissue over time, penetrating more quickly when gap fraction depends more strongly on depth. (d) The normalized standard deviation of concentration decreased over time, decreasing more quickly when gap fraction depends more strongly on depth. When gap fraction was independent of depth but changed from one simulation to the next, the tracer centroid penetrated deepest with a 2% gap fraction, regardless of time (e), and the normalized standard deviation was minimum for a gap fraction of 2% or 4% (f).

distribution, indicated by a smaller normalized standard deviation, given by

$$\frac{\sigma_C}{\bar{C}} = \frac{\sqrt{\sum_{i=1}^{n}(C_{i,\mathrm{in}} - \bar{C}_i)^2 + (C_{i,\mathrm{out}} - \bar{C}_i)^2}}{\bar{C}}, \tag{3.2}$$

where σ_C is the standard deviation of concentration and $C_{i,\mathrm{in}}$ and $C_{i,\mathrm{out}}$ represent the inlet and outlet concentrations in the ith segment, respectively.

With a steady inlet concentration of $C_0 = 100$ and an inlet pressure of 6.6 Pa (0.05 mmHg), we considered different gap distributions and different mean gap fractions. In all cases, $x_c = 0$, as expected from the symmetry of the model (figure 4a). Over time, y_c increased and z_c decreased as tracer spread out from the inlet, again matching our expectations (figure 4b,c). When the gap fraction power index was higher, y_c and z_c evolved more rapidly, indicating faster spread of tracer and better lateral perfusion. The normalized standard derivation of concentration dropped over time, as expected, since tracer was spreading from the inlet. When the gap fraction power index was higher, the standard deviation dropped more rapidly, indicating better perfusion (figure 4d). As the mean gap fraction was increased, the centroid height and the normalized standard deviation of concentration first decreased and then increased (figure 4e,f). A gap fraction around 2% minimized the centroid height and the normalized standard deviation, indicating optimal perfusion, which is consistent with the concentration measurement in figure 2.

3.4. Less-diffusive tracers exhibit better perfusion

Drugs and tracers have a broad range of molecular weights, from roughly 3 to 2000 kDa [12], which implies diffusivities ranging from 10 to 500 $\mu m^2\ s^{-1}$ [33,39]. With a steady inlet concentration of $C_0 = 100$ and an inlet velocity of $\approx 40\ \mu m\ s^{-1}$ at the mother pial PVS, we compared simulations with different diffusivities. We observed that a tracer with a low diffusivity of 10 $\mu m^2\ s^{-1}$ exhibited the most effective perfusion in the network, with its concentration depending only weakly on depth (figure 5a). In contrast, tracers with higher diffusivities (100 $\mu m^2\ s^{-1}$ in figure 5b and 2000 $\mu m^2\ s^{-1}$ in figure 5c) were quickly diluted in the ECS, resulting in lower mean concentrations in both the pial PVSs (figure 5d) and penetrating PVSs (figure 5e,f).

The finding that small-diffusivity tracers perfuse better is consistent with experiments by Iliff *et al.* [40], which examined deep penetrating PVS segments and found high concentrations of small-diffusivity tracers but not of large-diffusivity tracers. We emphasize that such observations (caused by dilution) are evidence of tracer transport into ECSs from PVSs: otherwise, all tracers would be transported into the smaller precapillary spaces, leaving the concentration unchanged.

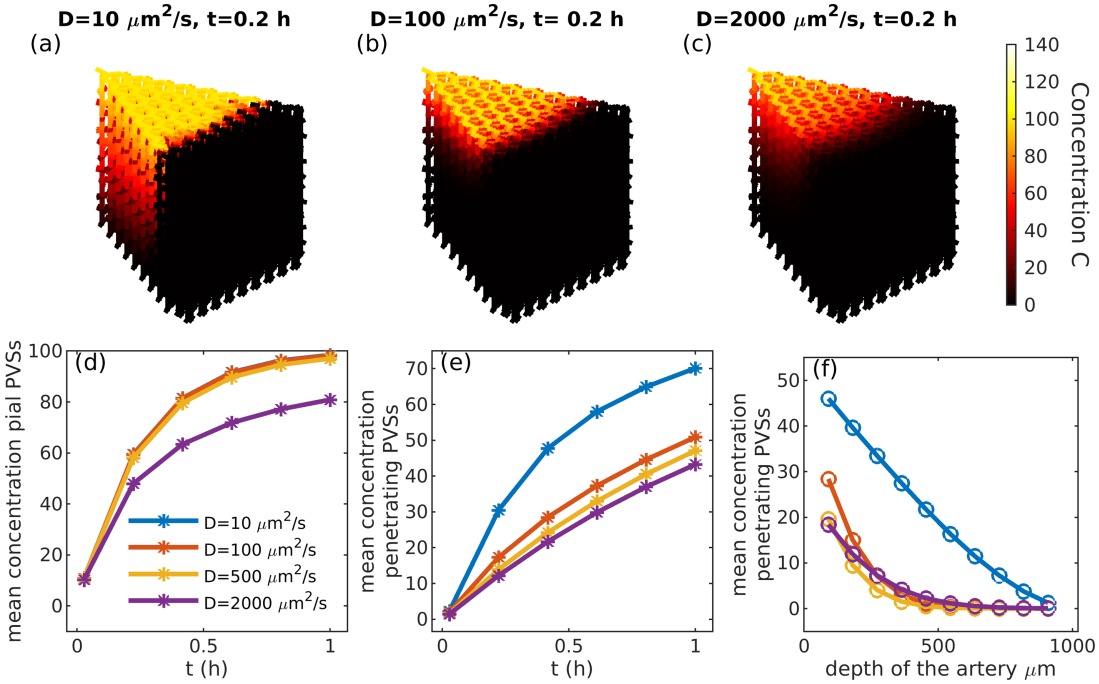

Figure 5. Perfusion with varying tracer diffusivities. (a–c) Simulated distribution at $t = 0.2$ h of tracers with various diffusivities. (d,e) With higher diffusivity, we found smaller mean tracer concentrations in the pial and penetrating PVSs. (f) At $t = 0.2$ h, concentration deep in the tissue is greater for large-diffusivity tracers than for small-diffusivity tracers.

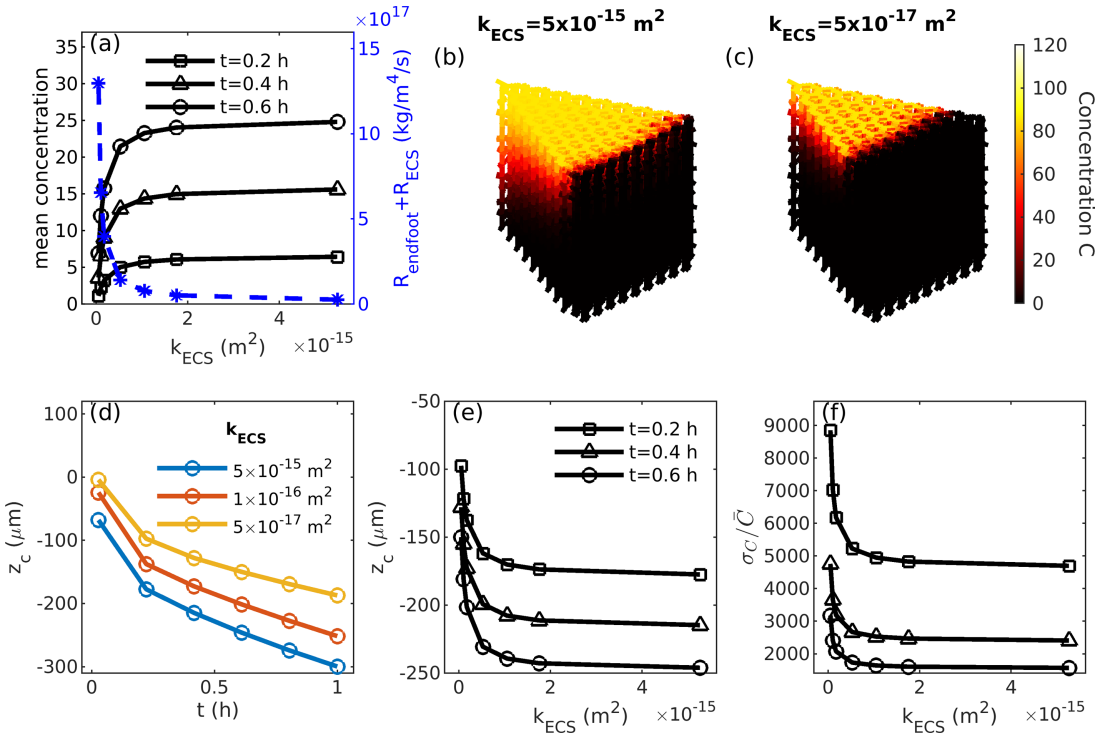

Figure 6. Perfusion with varying ECS permeabilities. (a) With a higher ECS permeability, the flow resistance decreases and the mean tracer concentration increases. Perfusion is better with higher ECS permeability (b) than with lower ECS permeability (c). (d,e) The tracer centroid penetrated deeper into the brain tissue with higher ECS permeability. (f) The normalized standard deviation decreased monotonically with ECS permeability.

3.5. Reduced extracellular space permeability suppresses perfusion

We performed simulations with different ECS permeabilities and a steady inlet concentration of $C_0 = 100$ and an inlet velocity of ≈ 40 μm s^{-1}. The flow resistance of the network decreased monotonically with the ECS permeability. As we increased the ECS permeability, we found higher mean tracer concentration (figure 6a). Increased ECS permeability also led to better perfusion (figure 6b,c). We also found that the centroid height and the normalized standard deviation decrease monotonically with ECS permeability, suggesting enhanced perfusion (figure 6d–f).

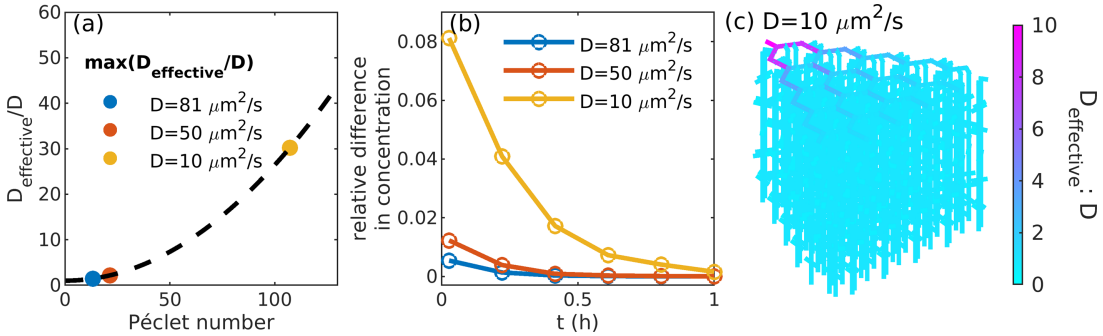

Figure 7. The effects of Taylor dispersion. (a) The diffusivity enhancement ratio, evaluated at the inlet PVS, increases with Péclet number. (b) The effect of Taylor dispersion on tracer concentration decreases over time and is weaker for tracers of higher diffusivity. (c) The diffusivity enhancement ratio is greatest near the inlet and small through most of the network.

3.6. The effect of Taylor dispersion

Taylor dispersion caused by the shear of the flow in a PVS can, in principle, enhance mixing and dispersion in the downstream direction of the flow [19]. Taylor dispersion plays a role at places where the PVS is open (not porous) [41], and the velocity varies over a cross section. Although our model is reduced to 1D, neglecting variations in velocity and solute concentration over cross section in PVSs, we can apply a correction to account for Taylor dispersion by increasing the effective downstream diffusion coefficient.

For an open PVS, modelled as a concentric annular tube, the leading-order governing equation for Taylor dispersion was derived by Aris [42] and reads

$$\frac{\partial \bar{C}(z,t)}{\partial t} + \bar{u}\frac{\partial \bar{C}(z,t)}{\partial z} = D_{\text{eff}}\frac{\partial^2 \bar{C}(z,t)}{\partial z^2}, \tag{3.3}$$

where $\bar{u}$ and $\bar{C}(z,t)$ are the velocity and concentration averaged over the cross section, $D_{\text{eff}} = D(1 + k\bar{u}^2(r_2^2 - r_1^2)/D^2)$ is the effective downstream diffusivity due to Taylor dispersion, D is the molecular diffusivity, r_1 and r_2 are the inner and outer radii of the PVS and k is a dimensionless constant determined by r_2/r_1 (also described in [20]). In the pial PVSs, which we know to be open, and the penetrating PVSs, which we assume to be open in our model, we can use equation (3.3) (instead of equation (2.1)) to estimate the effect of Taylor dispersion.

In figure 7a, we plot the ratio between the effective diffusion coefficient D_{eff} and the molecular diffusion coefficient D for the mother pial PVS (where the enhancement of dispersion is greatest due to the high flow velocity there) with respect to the Péclet number $Pe = \bar{u}(r_2 - r_1)/D$, following the approach in [20]. We find that tracers with a smaller molecular diffusivity exhibit a larger enhancement ratio, as Pe is proportional to $1/D$. We simulate the system with a tracer injection at the inlet, stopping the injection after 5 min and compare the maximum concentration in the network over time with a simulation that does not account for Taylor dispersion. The relative difference in concentrations between these two simulations is small and generally decreases over time (figure 7b). The difference is larger for tracers with a smaller molecular diffusivity. Figure 7c demonstrates that the enhancement of dispersion is significant in the first few pial PVSs in the network, where the flow speed is high, but becomes negligible in the remaining network where the flow is slower. At later times, as the solute distribution along the PVS becomes nearly uniform, Taylor dispersion becomes ineffective in altering the already uniform distribution (as pointed out in [11]).

Based on these results, we conclude that Taylor dispersion induced by steady shearing flows in the PVSs does not play an important role in solute transport in the network, at least over the time and length scales considered in our simulations.

4. Discussion

In this work, we have developed a semi-analytical network model to study time-dependent solute transport in the glymphatic system. We can calculate the leading-order concentration profile at any time and place in the model. We showed that results from our model closely matched results from a custom-made numerical solver.

Using this model, we found that maintaining small but reasonable gap fractions at the outer boundaries of penetrating PVSs near the brain's surface is crucial for solute perfusion. When the gap fraction was too large, tracer escaped into ECSs near the brain surface instead of reaching deeper regions of the brain. Conversely, when the gap fraction was too small, the high flow resistance reduced flow rates within penetrating PVSs, so tracer entered PVSs primarily through diffusion, which was too slow to ensure adequate perfusion. We found that a gap fraction around 2% maximizes perfusion, assuming a uniform gap width of 20 nm and an ECS permeability of 3.5×10^{-15} m^2. This optimal gap fraction falls within a reasonable range, as estimated by [34–36]. In Mestre *et al.* [17], the CSF tracer intensity along the penetrating PVSs remained uniform for at least 500 μm beneath the brain surface in wild-type mice, suggesting that the surface gap fraction is not too large. The aquaporin-4 water channels that decorate the astrocyte endfeet may decrease the flow resistance of the PVS outer wall. In aquaporin-4 knockout mice, CSF inflow was reduced and perfusion was no longer uniform through brain depth, which can be explained by a significantly increased flow resistance of the PVS outer wall, similar to the reasoning here that too small a gap fraction hinders the flow and suppresses perfusion. However, accurately measuring the gap fraction remains challenging because optical imaging cannot resolve such small spaces, and electron microscopy introduces substantial fixation artefacts [34].

We conducted simulations maintaining the same mean gap fraction but varying the spatial distribution. Specifically, we compared a simulation with a constant gap fraction to simulations where the gap fraction was proportional to tissue depth raised to the first, second and third powers. Our findings indicate that having a smaller gap fraction near the surface and a larger gap fraction in deeper brain regions enhances tracer perfusion. This result aligns with experimental measurements of gap dimensions and supports the model proposed by Wang *et al.* [18], who found that the endfoot size is proportional to the local vessel diameter. Because the diameter of penetrating arteries decreases with brain depth, endfoot size is also expected to decrease with depth, leading to increased gap fractions and, consequently, enhanced CSF perfusion. Also, the total number of gaps at a certain depth is proportional to n_{artery}, the number of branching arteries. Since the penetrating PVS undergoes approximately 11 bifurcations throughout its full depth and it barely bifurcates near the surface [22,43,44], the number of child arteries is expected to increase, leading to a rise in gap density in deeper brain regions, as modelled here.

We found that higher ECS permeability results in faster CSF flow and, thereby, better perfusion of tracer. Xie *et al.* [25] demonstrated that the permeability of the ECS is enhanced significantly during sleep and sleep-like states compared to wakefulness (see also [45]). Therefore, our simulations suggest that perfusion of solutes in the brain is enhanced during sleep and sleep-like states. Our result is also consistent with observations of minimum tracer intensity during wakefulness in injection experiments [12,25].

Furthermore, we found that tracers with lower diffusivity (heavier tracers) exhibit better perfusion across all depths of the brain. Due to their higher Péclet number, these tracers do not become diluted by diffusing rapidly at the surface of the brain parenchyma, so they penetrate tissue better. Finally, we found that Taylor dispersion—the enhanced dispersion induced by shear flow in open PVSs—does not play a significant role in this solute transport model, particularly at later times or for tracers with lower diffusivity.

Our semi-analytical solver uses Laplace transformations that are performed analytically, without any numerical approximations. However, the subsequent inverse Laplace transformations require numerical integrations in the frequency domain (Bromwich integrals). For those numerical integrations, the solver uses approximately 60 frequency samples, and we found the results to be more accurate than those of numerical spectral methods with as many as 3600 time steps. When the network contains n branches of PVS and parenchyma segments, each segment requires two boundary conditions. The computational cost of a conventional numerical method is approximately $O(2nml)$, where $m \approx 50$ is the number of spatial nodes per segment, and $l = T/\Delta t \approx 10^3$ is the number of time steps, scaling linearly with the end time T and inversely with the time step Δt. In contrast, for our semi-analytical solution, the computational cost at any time instant is only $O(2nk)$, where $k \approx 60$ is the number of frequencies used in the inverse Laplace transform. Moreover, each frequency can be computed independently, allowing parallel computation across CPUs. This effectively reduces the cost per CPU to $O(2n)$, whereas the numerical solver cannot be parallelized in time since each step depends on the previous solution. In short, the analytical framework is both more accurate and more computationally efficient compared to the numerical framework. The potential error in the former approach arises from the physical simplifications (i.e. dimensional reduction) rather than from the algorithm itself. Both solvers were implemented in MATLAB on a laboratory computer. The computational time for the analytical solver is five times smaller than the numerical solver per simulation using $\Delta t \approx 1\,s$.

Our model is subject to the following caveats. To derive the analytical solution, we assumed a steady flow in the network, neglecting the oscillatory component of the CSF flow [13]. However, arterial pulsations synchronized with the cardiac and potentially respiratory cycles are the primary drivers of CSF flow, which is inherently pulsatile and involves fluid–structure interactions [15]. Incorporating the direct coupling to solute transport would require equations with time-dependent coefficients and hence more advanced analytical techniques. With that being said, although the oscillatory component of the pulsation-driven flow can enhance solute mixing through Taylor dispersion [11,46], we have shown that its effect is insignificant at the large length and long time scales considered in the network (figure 7c). The current method can be modified for different steady or pulsatile fully developed flows by updating u in equations (2.1) and (2.2) [47]. The model does not incorporate any possible driving mechanisms of the flow [48–51], nor does it account for flow changes during the sleep–wake transition [25]. Also, the model is 1D, assuming all PVSs have concentric annular geometry, which is not accurate. We computed the flow flux entering evenly spaced parenchyma nodes along the penetrating PVS axis to model continuous fluid loss through the PVS outer wall. While this 1D simplification captures axial pressure and velocity profiles resulting from fluid exchange with the surrounding tissue, a future extension to a 2D advection–diffusion model with a leaky boundary would better represent the inherently 2D nature of the problem [42,52,53]. We restricted advection and diffusion in the ECS to only the radial direction, neglecting transport parallel to the penetrating arterioles. Although others have also made similar simplifications [54] to derive comparable analytical solutions, transport in the axial direction within the ECS may play a significant role, particularly in waste clearance. Axial advection and diffusion in the ECS can redistribute waste proteins that are uniformly produced in the ECS, thereby enhancing their clearance. The model is computationally inexpensive, at the cost of sacrificing fidelity compared to the models of [55–57].

Furthermore, the efflux pathways of the glymphatic system remain poorly characterized, introducing uncertainty and limitations to our model. Multiple routes—including surface and meningeal lymphatic vessels, SASs, perivenous spaces and periarterial basement membranes—may each contribute to solute clearance. The solute transport varies with spatial location and the resistance of the efflux pathways. For instance, efflux routes at the brain surface, such as the SAS and meningeal lymphatics, may remove a substantial portion of solute tracers, thereby reducing tracer influx to the parenchyma and leading to poor perfusion. Future studies that identify and characterize the efflux pathways are necessary.

Several parameters in the network model are highly uncertain, such as the permeabilities of the parenchyma and the penetrating PVSs. The existence and characteristics of capillary PVSs have yet to be determined. Certain parameter choices may lead to unrealistic concentration profiles, and future studies that compare the simulated concentration over time for different parameters with previous *in vivo* measurements of global solute transport could help constrain these uncertainties. Future efforts, such as

performing sensitivity analysis [7] or Bayesian inference [58] on this low-computational cost model, could further advance our understanding.

Our model can be extended to compare solute transport between disease and control conditions. In mice with cerebral amyloid angiopathy, CSF flow in the surface pial PVSs has been observed to be faster, whereas global glymphatic transport is reduced by approximately 15% [59,60]. This apparent paradox may be explained by the poor perfusion we observed when the surface gap fraction becomes excessively large and the local flow is high (figure 2c,d). In such cases, a major portion of the solute is rapidly advected by the fast surface flow and fails to penetrate into the deeper brain regions. Beyond gap fraction changes, other factors that may alter flow distribution within the network can also be incorporated into the model—for example, increased arterial tortuosity observed in disease states.

Our model can also be used to guide and interpret experiments, such as trials of brain drug delivery through the glymphatic pathway. Efforts to modulate CSF influx with ultrasound stimulation [61], multisensory gamma stimulation [62] or optogenetic stimulation [12,63], often rely on tracer injection experiments and concentration measurements in mouse brains; our model might be applied to such modulations. CSF flow in the mouse brain and the human brain is often measured by tracking solute using magnetic resonance imaging [64,65]. Comparing the simulations from our model with such experiments could help us better understand hidden mechanisms. Beyond the brain, the model could be readily adapted to investigate global solute transport in other organs, such as the liver [66].

Ethics. This work did not require ethical approval from a human subject or animal welfare committee.

Data accessibility. Simulation code with sample parameter sets and visualization code is available at Zenodo [67].

Declaration of AI use. We used ChatGPT for a grammar check.

Authors' contributions. Y.G.: conceptualization, investigation, methodology, software, validation, visualization, writing—original draft; K.Q.: conceptualization, methodology, software, writing—review and editing; K.S.B.: methodology, supervision, writing—review and editing; J.H.T.: methodology, supervision, writing—review and editing; D.H.K.: funding acquisition, project administration, supervision, writing—review and editing.

All authors gave final approval for publication and agreed to be held accountable for the work performed therein.

Conflict of interest declaration. We declare we have no competing interests.

Funding. This research was supported by the US Army (grant no. MURI W911NF1910280), by the US National Center for Complementary and Integrative Health (grant no. R01AT012312) and by the BRAIN Initiative of the US National Institutes of Health (grant no. U19NS128613).

Acknowledgements. We thank Antonio Ladrón de Guevara Ruiz, Ibrahim Mohammad and Yisen Guo for valuable discussions. We thank Jeff Tithof for help with the network model.

Appendix A. The numerical solver

The implicit discrete form of the advection–diffusion equation (2.1) for the solute transport in the PVSs is

$$\frac{C^{n+1}-C^n}{\Delta t}+uD_zC^{n+1}-DD_z^2C^{n+1}=0, \tag{A 1}$$

where n represents the nth time step and D_z is the Chebyshev differentiation matrix [52,68]. Rewriting equation (A 1), we have

$$\left(\mathbf{I}+\Delta t(uD_z-DD_z^2)\right)C^{n+1}=C^n, \tag{A 2}$$

where $\mathbf{I}$ is the identity matrix of the same size as D_z.

The implicit discrete form for the solute transport in the parenchyma equation (2.2) reads

$$\frac{C^{n+1}-C^n}{\Delta t}+\left(\frac{m-2\pi D_{\text{eff}}}{2\pi r}\right)D_rC^{n+1}-D_{\text{eff}}D_r^2C^{n+1}=0, \tag{A 3}$$

where D_r is the differentiation matrix. Rewriting equation (A 3), we have

$$\left(\mathbf{I}+\Delta t\left(\frac{m-2\pi D_{\text{eff}}}{2\pi r}D_r-D_{\text{eff}}D_r^2\right)\right)C^{n+1}=C^n. \tag{A 4}$$

Appendix B. Semi-analytical solution of solute transport in the parenchyma

The governing advection–diffusion equation for the solute transport in the parenchyma reads

$$\frac{\partial C}{\partial t}+\frac{q}{2\pi r}\frac{\partial C}{\partial r}=D_{\text{eff}}\left(\frac{\partial^2C}{\partial r^2}+\frac{1}{r}\frac{\partial C}{\partial r}\right). \tag{B 1}$$

Its Laplace transform is

$$\frac{\partial^2\hat{C}}{\partial R^2}+\mu\frac{1}{R}\frac{\partial\hat{C}}{\partial R}+\hat{C}=0, \tag{B 2}$$

where $R=r\sqrt{-\frac{s}{D_{\text{eff}}}}$ and $\mu=\frac{D_{\text{eff}}-\frac{q}{2\pi}}{D_{\text{eff}}}$. Letting $\hat{C}=\hat{M}R^k$, where $k=\frac{1-\mu}{2}=\frac{q}{4\pi D}$, and rearranging leads to

$$(R^2-k^2)\hat{M}+\frac{1}{R}\frac{\partial\hat{M}}{\partial R}+\frac{\partial^2\hat{M}}{\partial R^2}=0, \tag{B 3}$$

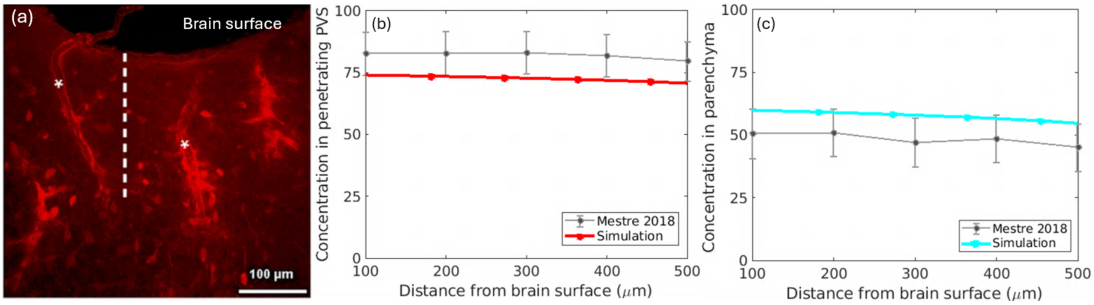

Figure 8. (a) Image of a mouse brain, 30 min after a 3 kDa dextran injection [17]. Fluorescent intensity in arbitrary units was measured in penetrating PVSs, identified by asterisks, and at least 50 μm into parenchymal tissue, identified by a dashed line. (b) A comparison of the experimentally measured fluorescent intensity (grey) to simulated concentrations in penetrating PVSs (red) 30 min after dye injection. (c) A comparison of the experimentally measured fluorescent intensity (grey) to simulated concentrations at parenchymal outlets (cyan) 30 min after dye injection. Experimental measurements are plotted with error bars indicating the standard deviation of measurements in different wild-type mice. Simulations use a pressure drop such that the velocity along anterior third the pial surface matches the previously measured pial velocity of 18.7 m s^{-1} [10,17]. When applying realistic conditions to velocities in the network, the model can accurately reproduce solute transport over time.

which is a Bessel differential equation, and the general solution for $\hat{M}$ is

$$\hat{M} = A_1 J_k(R) + A_2 Y_k(R), \tag{B 4}$$

and the general solution for $\hat{C}$ is

$$\hat{C}(r,s) = A_1 \left(r\sqrt{-\frac{s}{D_{\text{eff}}}} \right)^k J_k\left(r\sqrt{-\frac{s}{D_{\text{eff}}}} \right) + A_2 \left(r\sqrt{-\frac{s}{D_{\text{eff}}}} \right)^k Y_k\left(r\sqrt{-\frac{s}{D_{\text{eff}}}} \right), \tag{B 5}$$

where J_k is the kth Bessel function of the first kind, Y_k is the kth Bessel function of the second kind and the coefficients A_1 and A_2 are determined by the boundary conditions at the inlet and outlet of the parenchyma.

The volumetric average concentration reads

$$\begin{aligned} \bar{\hat{C}} = \frac{2\pi L \int_{r_1}^{r_2} r\hat{C}(r,s)\mathrm{d}r}{V} = \frac{2\pi L}{V}\sqrt{-\frac{D_{\text{eff}}}{s}} \Bigg(& A_1 \left(r\sqrt{-\frac{s}{D_{\text{eff}}}} \right)^{k+1} J_{k+1}\left(r\sqrt{-\frac{s}{D_{\text{eff}}}} \right) \\ & + A_2 \left(r\sqrt{-\frac{s}{D_{\text{eff}}}} \right)^{k+1} Y_{k+1}\left(r\sqrt{-\frac{s}{D_{\text{eff}}}} \right) \Bigg) \Bigg|_{r=r_1}^{r=r_2}, \end{aligned} \tag{B 6}$$

where r_1 and r_2 are the radii of the inner and outer boundaries of the ECS, respectively, L is its axial length, and V is its volume.

The following properties of Bessel functions are utilized to calculate the integral in equation (B 6) and the derivative in equation (2.4):

$$\begin{aligned} \frac{\mathrm{d}(r^k J_k(r))}{\mathrm{d}r} &= r^{k-1} J_{k-1}(r), \\ \frac{\mathrm{d}(r^k Y_k(r))}{\mathrm{d}r} &= r^{k-1} Y_{k-1}(r). \end{aligned} \tag{B 7}$$

Appendix C. Comparison with experiment

To confirm that the network model can accurately reproduce the solute transport properties observed in animals, we simulated a 3 kDa dextran injection performed by Mestre *et al.* [17]. In this experiment, the dye was administered for 5 min and the mice were sacrificed 30 min after injection. To simulate this scenario, a high concentration is held fixed at the inlet of the network for 30 min. The results of one such simulation are shown in figure 8b,c. The parameter values are the same as those shown in figure 1, using the lower bound of parenchymal permeability and a gap fraction that is proportional to $-z^5$. The diffusion coefficient for 3 kDa dextran is 2.33×10^{-10} m^2 s^{-1}. The change in concentration with depth is similar between the experimental and simulated cases, demonstrating that the model can exhibit realistic behaviour.

Appendix D. Check of the simplified model

In order to simplify the network and enable an analytical solution, we have modelled the fluid exchange between the PVS and the parenchyma by calculating the flux into 11 evenly spaced parenchyma nodes along each penetrating PVS. However, in reality, this fluid exchange is continuous through all the endfoot gaps on the PVS outer wall, which poses an inherently 2D problem. Increasing the number of 1D parenchymal nodes should better approximate the 2D problem. Therefore, to justify the simplification, we performed simulations with different numbers of parenchymal nodes per PVS using a hexagon model. We found that the concentration profiles are similar (figure 9a,b). We also found that the pressure distributions (with depth) converge as we increase the

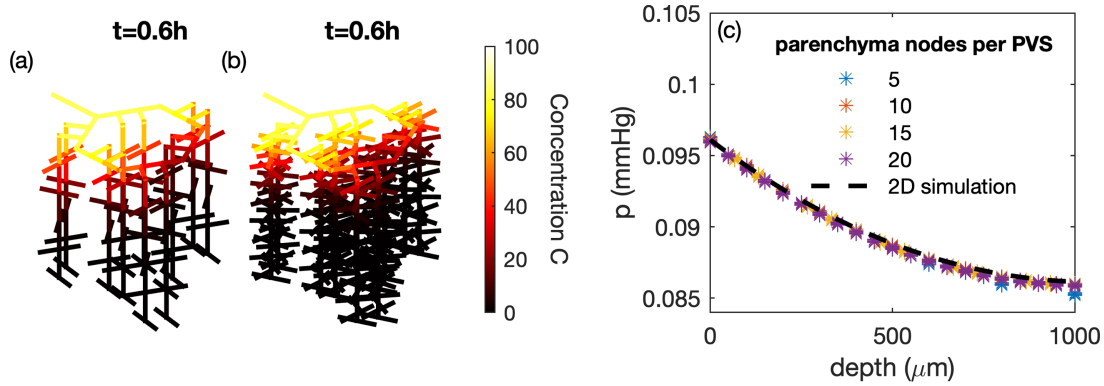

Figure 9. Comparison of simulations with different numbers of parenchymal nodes per penetrating PVS using a one-generation hexagon model. (a) Concentration profile at $t = 0.6$ h for the simulation with five nodes per PVS. (b) Concentration profile at $t = 0.6$ h for the simulation with 15 nodes per PVS. (c) As we increase the number of nodes per PVS, the pressure converges to the cross-sectional average pressure computed from a 2D simulation using lubrication theory, in which fluid leaks through endfoot gaps continuously along the penetrating PVS.

number of nodes (figure 9c). The converged pressure distribution matched the distribution of cross-sectional averaged pressure obtained from a 2D simulation using lubrication theory [52], in which the fluid exchange through the endfoot gaps is continuous along the outer wall and the same pressures are applied at the inlet and outlet of the penetrating PVS.

References

1. Smyth LCD *et al*. 2024 Identification of direct connections between the dura and the brain. *Nature* **627**, 165–173. (doi:10.1038/s41586-023-06993-7)
2. Tithof J, Kelley DH, Mestre H, Nedergaard M, Thomas JH. 2019 Hydraulic resistance of periarterial spaces in the brain. *Fluids Barriers CNS* **16**, 19. (doi:10.1186/s12987-019-0140-y)
3. Kelley DH, Thomas JH. 2023 Cerebrospinal fluid flow. *Annu. Rev. Fluid Mech.* **55**, 237–264. (doi:10.1146/annurev-fluid-120720-011638)
4. Rossinelli D, Fourestey G, Killer HE, Neutzner A, Iaccarino G, Remonda L, Berberat J. 2024 Large-scale in-silico analysis of CSF dynamics within the subarachnoid space of the optic nerve. *Fluids Barriers CNS* **21**, 20. (doi:10.1186/s12987-024-00518-8)
5. Mathiesen BK *et al*. 2023 Delivery of gene therapy through a cerebrospinal fluid conduit to rescue hearing in adult mice. *Sci. Transl. Med.* **15**, 916. (doi:10.1126/scitranslmed.abq3916)
6. Tithof J, Boster KAS, Bork PAR, Nedergaard M, Thomas JH, Kelley DH. 2022 A network model of glymphatic flow under different experimentally-motivated parametric scenarios. *iScience* **25**, 104258. (doi:10.1016/j.isci.2022.104258)
7. Boster KAS, Tithof J, Cook DD, Thomas JH, Kelley DH. 2022 Sensitivity analysis on a network model of glymphatic flow. *J. R. Soc. Interface* **19**, 20220257. (doi:10.1098/rsif.2022.0257)
8. Faghih MM, Sharp MK. 2018 Is bulk flow plausible in perivascular, paravascular and paravenous channels? *Fluids Barriers CNS* **15**, 17. (doi:10.1186/s12987-018-0103-8)
9. Blinder P, Shih AY, Rafie C, Kleinfeld D. 2010 Topological basis for the robust distribution of blood to rodent neocortex. *Proc. Natl Acad. Sci. USA* **107**, 12670–12675. (doi:10.1073/pnas.1007239107)
10. Quirk K, Boster KAS, Tithof J, Kelley DH. 2024 A brain-wide solute transport model of the glymphatic system. *J. R. Soc. Interface* **21**, 20240369. (doi:10.1098/rsif.2024.0369)
11. Thomas JH. 2019 Fluid dynamics of cerebrospinal fluid flow in perivascular spaces. *J. R. Soc. Interface* **16**, 20190572. (doi:10.1098/rsif.2019.0572)
12. Holstein-Rønsbo S *et al*. 2023 Glymphatic influx and clearance are accelerated by neurovascular coupling. *Nat. Neurosci.* **26**, 1042–1053. (doi:10.1038/s41593-023-01327-2)
13. Mestre H *et al*. 2018 Flow of cerebrospinal fluid is driven by arterial pulsations and is reduced in hypertension. *Nat. Commun.* **9**, 4878. (doi:10.1038/s41467-018-07318-3)
14. Ringstad G, Valnes LM, Dale AM, Pripp AH, Vatnehol SAS, Emblem KE, Mardal KA, Eide PK. 2018 Brain-wide glymphatic enhancement and clearance in humans assessed with MRI. *JCI Insight* **3**, e121537. (doi:10.1172/jci.insight.121537)
15. Taoka T, Masutani Y, Kawai H, Nakane T, Matsuoka K, Yasuno F, Kishimoto T, Naganawa S. 2017 Evaluation of glymphatic system activity with the diffusion MR technique: diffusion tensor image analysis along the perivascular space (DTI-ALPS) in Alzheimer's disease cases. *Jpn. J. Radiol.* **35**, 172–178. (doi:10.1007/s11604-017-0617-z)
16. Eide PK, Vinje V, Pripp AH, Mardal KA, Ringstad G. 2021 Sleep deprivation impairs molecular clearance from the human brain. *Brain (Bacau)* **144**, 863–874. (doi:10.1093/brain/awaa443)
17. Mestre H *et al*. 2018 Aquaporin-4-dependent glymphatic solute transport in the rodent brain. *eLife* **7**, e40070. (doi:10.7554/eLife.40070)
18. Wang MX, Ray L, Tanaka KF, Iliff JJ, Heys J. 2021 Varying perivascular astroglial endfoot dimensions along the vascular tree maintain perivascular-interstitial flux through the cortical mantle. *Glia* **69**, 715–728. (doi:10.1002/glia.23923)
19. Taylor GI. 1953 Dispersion of soluble matter in solvent flowing slowly through a tube. *Proc. R. Soc. Lond. A* **219**, 186–203. (doi:10.1098/rspa.1953.0139)
20. Troyetsky DE, Tithof J, Thomas JH, Kelley DH. 2021 Dispersion as a waste-clearance mechanism in flow through penetrating perivascular spaces in the brain. *Sci. Rep.* **11**, 4595. (doi:10.1038/s41598-021-83951-1)
21. Hannocks MJ, Pizzo ME, Huppert J, Deshpande T, Abbott NJ, Thorne RG, Sorokin L. 2018 Molecular characterization of perivascular drainage pathways in the murine brain. *J. Cereb. Blood Flow Metab.* **38**, 669–686. (doi:10.1177/0271678X17749689)
22. Blinder P, Tsai PS, Kaufhold JP, Knutsen PM, Suhl H, Kleinfeld D. 2013 The cortical angiome: an interconnected vascular network with noncolumnar patterns of blood flow. *Nat. Neurosci.* **16**, 889–897. (doi:10.1038/nn.3426)
23. Landau LD. 2013 *Fluid mechanics: Landau and Lifshitz: course of theoretical physics*, vol. 6. Amsterdam, The Netherlands: Elsevier.
24. Schreder HE, Liu J, Kelley DH, Thomas JH, Boster KAS. 2022 A hydraulic resistance model for interstitial fluid flow in the brain. *J. R. Soc. Interface* **19**, 20210812. (doi:10.1098/rsif.2021.0812)
25. Xie L *et al*. 2013 Sleep drives metabolite clearance from the adult brain. *Science* **342**, 373–377. (doi:10.1126/science.1241224)
26. Bakker ENTP, Naessens DMP, VanBavel E. 2019 Paravascular spaces: entry to or exit from the brain? *Exp. Physiol.* **104**, 1013–1017. (doi:10.1113/EP087424)

27. Hu J, Shen Y, Fahmy LM, Krishnamurthy S, Li J, Zhang L, Chen Y, Haacke EM, Jiang Q. 2023 The role of the parenchymal vascular system in cerebrospinal fluid tracer clearance. *Eur. Radiol.* **33**, 656–665. (doi:10.1007/s00330-022-09022-9)
28. Valsa J, Brančik L. 1998 Approximate formulae for numerical inversion of Laplace transforms. *Int. J. Numer. Model.* **11**, 153–166. (doi:10.1002/(SICI)1099-1204(199805/06)11:3<153::AID-JNM299>3.0.CO;2-C)
29. Mestre H, Kostrikov S, Mehta RI, Nedergaard M. 2017 Perivascular spaces, glymphatic dysfunction, and small vessel disease. *Clin. Sci.* **131**, 2257–2274. (doi:10.1042/CS20160381)
30. Yurchenco PD. 2011 Basement membranes: cell scaffoldings and signaling platforms. *Cold Spring Harb. Perspect. Biol.* **3**, a004911. (doi:10.1101/cshperspect.a004911)
31. Miyawaki T, Morikawa S, Susaki EA, Nakashima A, Takeuchi H, Yamaguchi S, Ueda HR, Ikegaya Y. 2020 Visualization and molecular characterization of whole-brain vascular networks with capillary resolution. *Nat. Commun.* **11**, 1104. (doi:10.1038/s41467-020-14786-z)
32. Basser PJ. 1992 Interstitial pressure, volume, and flow during infusion into brain tissue. *Microvasc. Res.* **44**, 143–165. (doi:10.1016/0026-2862(92)90077-3)
33. Holter KE *et al*. 2017 Interstitial solute transport in 3D reconstructed neuropil occurs by diffusion rather than bulk flow. *Proc. Natl Acad. Sci. USA* **114**, 9894–9899. (doi:10.1073/pnas.1706942114)
34. Mathiisen TM, Lehre KP, Danbolt NC, Ottersen OP. 2010 The perivascular astroglial sheath provides a complete covering of the brain microvessels: an electron microscopic 3D reconstruction. *Glia* **58**, 1094–1103. (doi:10.1002/glia.20990)
35. Koch T, Vinje V, Mardal KA. 2023 Estimates of the permeability of extra-cellular pathways through the astrocyte endfoot sheath. *Fluids Barriers CNS* **20**, 20. (doi:10.1186/s12987-023-00421-8)
36. KorogodN P, KnottGW GW. 2015 Ultrastructural analysis of adult mouse neocortex comparing aldehyde perfusion with cryo fixation. *eLife* **4**, 05793. (doi:10.7554/eLife.05793)
37. Kestin J, Sokolov M, Wakeham WA. 1978 Viscosity of liquid water in the range −8 °C to 150 °C. *J. Phys. Chem. Ref. Data* **7**, 941–948. (doi:10.1063/1.555581)
38. NicholsonC C, HrabětováS T. 2000 Diffusion of molecules in brain extracellular space. *Theory Exp.* **125**, 129–154. (doi:10.1016/S0079-6123(00)25007-3)
39. Syková E, Nicholson C. 2008 Diffusion in brain extracellular space. *Physiol. Rev.* **88**, 1277–1340. (doi:10.1152/physrev.00027.2007)
40. Iliff JJ *et al*. 2012 A paravascular pathway facilitates CSF flow through the brain parenchyma and the clearance of interstitial solutes, including amyloid β. *Sci. Transl. Med.* **4**, 147–111. (doi:10.1126/scitranslmed.3003748)
41. Min Rivas F, Liu J, Martell BC, Du T, Mestre H, Nedergaard M, Tithof J, Thomas JH, Kelley DH. 2020 Surface periarterial spaces of the mouse brain are open, not porous. *J. R. Soc. Interface* **17**, 20200593. (doi:10.1098/rsif.2020.0593)
42. Aris R. 1959 On the dispersion of a solute by diffusion, convection and exchange between phases. *Proc. R. Soc. Lond. A* **252**, 538–550. (doi:10.1098/rspa.1959.0171)
43. Kedarasetti RT, Drew PJ, Costanzo F. 2022 Arterial vasodilation drives convective fluid flow in the brain: a poroelastic model. *Fluids Barriers CNS* **19**, 34. (doi:10.1186/s12987-022-00326-y)
44. He XZ *et al*. 2022 High-resolution 3D demonstration of regional heterogeneity in the glymphatic system. *J. Cereb. Blood Flow Metab.* **42**, 2017–2031. (doi:10.1177/0271678X221109997)
45. Thomas JH. 2019 Theoretical analysis of wake/sleep changes in brain solute transport suggests a flow of interstitial fluid. *Fluids Barriers CNS* **19**, 30. (doi:10.1186/s12987-022-00325-z)
46. Wang B, Jiang W, Zeng L, Wu Z, Wang P. 2025 Taylor–Aris dispersion of active particles in oscillatory channel flows. *J. Fluid Mech.* **1021**, A3. (doi:10.1017/jfm.2025.10700)
47. Bakker LMML, Xiao N, van de Ven AAF, Schaap M, van de Vosse FN, Taylor CA. 2021 Image-based blood flow estimation using a semi-analytical solution to the advection–diffusion equation in cylindrical domains. *J. Fluid Mech.* **924**, 18. (doi:10.1017/jfm.2021.596)
48. Carr JB, Thomas JH, Liu J, Shang JK. 2021 Peristaltic pumping in thin non-axisymmetric annular tubes. *J. Fluid Mech.* **917**, A10. (doi:10.1017/jfm.2021.277)
49. Bork PAR, Ladrón-de-Guevara A, Christensen AH, Jensen KH, Nedergaard M, Bohr T. 2023 Astrocyte endfeet may theoretically act as valves to convert pressure oscillations to glymphatic flow. *J. R. Soc. Interface* **20**, 20230050. (doi:10.1098/rsif.2023.0050)
50. Gan Y, Holstein-Rønsbo S, Nedergaard M, Boster KAS, Thomas JH, Kelley DH. 2023 Perivascular pumping of cerebrospinal fluid in the brain with a valve mechanism. *J. R. Soc. Interface* **20**, 20230288. (doi:10.1098/rsif.2023.0288)
51. Gan Y, Thomas JH, Kelley DH. 2024 Gaps in the wall of a perivascular space act as valves to produce a directed flow of cerebrospinal fluid: a hoop-stress model. *J. R. Soc. Interface* **21**, 20230659. (doi:10.1098/rsif.2023.0659)
52. Romanò F, Suresh V, Galie PA, Grotberg JB. 2020 Peristaltic flow in the glymphatic system. *Sci. Rep.* **10**, 21065. (doi:10.1038/s41598-020-77787-4)
53. Griffiths IM, Howell PD, Shipley RJ. 2013 Control and optimization of solute transport in a thin porous tube. *Phys. Fluids* **25**, 033101. (doi:10.1063/1.4795545)
54. Dejam M, Hassanzadeh H. 2021 The role of a porous wall on the solute dispersion in a concentric annulus. *Phys. Fluids* **33**, 116602. (doi:10.1063/5.0070653)
55. Vinje V, Zapf B, Ringstad G, Eide PK, Rognes ME, Mardal KA. 2023 Human brain solute transport quantified by glymphatic MRI-informed biophysics during sleep and sleep deprivation. *Fluids Barriers CNS* **20**, 62. (doi:10.1186/s12987-023-00459-8)
56. Bojarskaite L, Vallet A, Bjørnstad DM, Gullestad Binder KM, Cunen C, Heuser K, Kuchta M, Mardal KA, Enger R. 2023 Sleep cycle-dependent vascular dynamics in male mice and the predicted effects on perivascular cerebrospinal fluid flow and solute transport. *Nat. Commun.* **14**, 953. (doi:10.1038/s41467-023-36643-5)
57. Yousofvand R, Tithof J. 2025 Numerical simulations reveal complementary function of blood-brain barrier and glymphatic transport in the brain. *Phys. Rev. Lett.* **134**, 138403. (doi:10.1103/PhysRevLett.134.138403)
58. Schäfer A, Peirlinck M, Linka K, Kuhl E. 2021 Bayesianbayesian physics-based modeling of tau propagation in Alzheimer's disease. *Front. Physiol.* **12**, 702975. (doi:10.3389/fphys.2021.702975)
59. Che X, Liu X, Koundal S. 2022 Cerebral amyloid angiopathy is associated with glymphatic transport reduction and time-delayed solute drainage along the neck arteries. *Nat. Aging* **2**, 214–223. (doi:10.1038/s43587-022-00181-4)
60. Hirschler L *et al*. 2025 Region-specific drivers of CSF mobility measured with MRI in humans. *Nat. Neurosci.* **28**, 2392–2401. (doi:10.1038/s41593-025-02073-3)
61. Yoo SS, Kim HC, Kim J, Kim E, Kowsari K, Van Reet J, Yoon K. 2022 Enhancement of cerebrospinal fluid tracer movement by the application of pulsed transcranial focused ultrasound. *Sci. Rep.* **12**, 12940. (doi:10.1038/s41598-022-17314-9)
62. Murdock MH *et al*. 2024 Multisensory gamma stimulation promotes glymphatic clearance of amyloid. *Nature* **627**, 149–156. (doi:10.1038/s41586-024-07132-6)
63. Jiang-Xie LF, Drieu A, Bhasiin K, Quintero D, Smirnov I, Kipnis J. 2024 Neuronal dynamics direct cerebrospinal fluid perfusion and brain clearance. *Nature* **627**, 157–164. (doi:10.1038/s41586-024-07108-6)
64. Zhu Y *et al*. 2023 Transport pathways and kinetics of cerebrospinal fluid tracers in mouse brain observed by dynamic contrast-enhanced MRI. *Sci. Rep.* **13**, 13882. (doi:10.1038/s41598-023-40896-x)
65. Wright AM, Wu YC, Yang HC, Risacher SL, Saykin AJ, Tong Y, Wen Q. 2024 Coupled pulsatile vascular and paravascular fluid dynamics in the human brain. *Fluids Barriers CNS* **21**, 71. (doi:10.1186/s12987-024-00572-2)

66. Tithof J, Pruett TL, Rao JS. 2023 Lumped parameter liver simulation to predict acute haemodynamic alterations following partial resections. *J. R. Soc. Interface* **20**, 20230444. (doi:10.1098/rsif.2023.0444)
67. Gan Y. 2025 Network model of time-dependent solute transport in the brain. Zenodo. (doi:10.5281/zenodo.16996736)
68. Fortunato D. 2024 A high-order fast direct solver for surface PDEs. *SIAM J. Sci. Comput.* **46**, 2582–2606. (doi:10.1137/22M1525259)